# Cell class-specific electric field entrainment of neural activity

Soo Yeun Lee[1], Fahimeh Baftizadeh[1], Luke Campagnola[1], Tim Jarsky[1], Christof Koch[1], Costas A. Anastassiou[2, 3, 4, 5, 6]

[1]Allen Institute for Brain Science, Seattle, Washington 98101, USA
[2]Department of Neurosurgery, Cedars-Sinai Medical Center, Los Angeles, California 90048, USA
[3]Department of Neurology, Cedars-Sinai Medical Center, Los Angeles, California 90048, USA
[4]Board of Governors Regenerative Medicine Institute, Cedars-Sinai Medical Center, Los Angeles, California 90048, USA
[5]Center for Neural Science and Medicine, Department of Biomedical Sciences, Cedars-Sinai Medical Center, Los Angeles, California 90048, USA

[6]Lead contact: costas.anastassiou@cshs.org
*Correspondence: costas.anastassiou@cshs.org, sooyl@alleninstitute.org

**Abstract**

Electric fields affect the activity of neurons and brain circuits, yet how this interaction happens at the cellular level remains enigmatic. Lack of understanding on how to stimulate the human brain to promote or suppress specific activity patterns significantly limits basic research and clinical applications. Here we study how electric fields impact the subthreshold and spiking properties of major cortical neuronal classes. We find that cortical neurons in rodent neocortex and hippocampus as well as human cortex exhibit strong and cell class-dependent entrainment that depends on the stimulation frequency. Excitatory pyramidal neurons with their typically slower spike rate entrain to slow and fast electric fields, while inhibitory classes like Pvalb and SST with their fast spiking predominantly phase lock to fast fields. We show this spike-field entrainment is the result of two effects: non-specific membrane polarization occurring across classes and class-specific excitability properties. Importantly, these properties of spike-field and class-specific entrainment are present in cells across cortical areas and species (mouse and human). These findings open the door to the design of selective and class-specific neuromodulation technologies.

## Introduction

Delivery of exogenous electric fields of various shapes and forms through stimulation devices to alter brain activity has a rich history in neuroscience. Since the early work by Fritsch and Hitzig mapping brain region during surgery [1,2], extracellular electric stimulation (ES) has been used to measure functional connectivity, excitability and response properties of the brain. In therapeutic interventions, ES alleviates symptoms of neurological disorders such as Parkinson's disease[3–5], dystonia[6], depression[7–9], epilepsy [10,11] and others (e.g. see review [12]). Despite these advances, there is still a lack of understanding at the basic cellular level of what happens when brain matter is electrically stimulated to promote certain activity patterns or suppress others [13–17]. This has limited the application of ES as a basic science tool and, importantly, as a therapeutic intervention for brain disorders.

Brain circuits consist of multiple distinct and diverse cell classes yet how ES affects these classes individually at a cellular level remains unknown. Most studies of ES focus on the excitatory glutamatergic neurons in various brain regions (neocortex [18,19,17]; hippocampus [20–23]; but also [24–26]). While inhibitory GABAergic cells are less in absolute numbers, they play critical roles in structuring and regulating brain circuit activity [27–31]. Given such diversity, whether and how ES impacts excitatory and inhibitory classes in the cortical circuit remains unclear, as well as the extent to which class-specificity can be achieved using ES. For example, it is unclear whether inhibitory classes entrain to the ES like excitatory neurons, or whether they remain unperturbed due to their morphological compactness [16,32]. As a result, ES protocols applied in the brain of both animal models and humans do so without consideration for the remarkable cellular diversity comprising brain circuits.

Here we study the direct impact of extracellular ES in two cortical brain regions, visual cortex and CA1 hippocampus, using simultaneous intracellular (whole-cell patch-clamp) and extracellular recordings from identified single neurons of major excitatory and inhibitory cell classes. We observe strong, differential and cell class-specific spike-field entrainment with excitatory neurons entraining already at slow ES frequencies (8 Hz) while inhibitory neurons only entraining for fast ES frequencies (30-140 Hz). We also show that the class-dependence of spike entrainment is not the result of a differential subthreshold (i.e., non-spiking) effect as cortical neurons across classes, brain regions and, in fact, species exhibit ubiquitous, robust, and frequency-independent membrane coupling to ES oscillations. The fact that we see similar entrainment properties in human excitatory cortical neurons suggests a widely present, ion-independent biophysical mechanism of field entrainment that, in principle, allows for the selective stimulation of distinct classes. The latter opens the door to the design of new ES waveforms and delivery systems offering improved selectivity and neural control.

## Results

To simultaneously stimulate and record intracellular and extracellular signals close to identified neurons, we use an *in vitro* experimental setup to examine the cellular and cell-class-specific effects of the electric stimulation (**ES**)-generated field, at multiple locations around the cell body. To achieve positioning multiple stimulation and recording sites in specific locations near a cell body we used a customized 8-pipette multipatch brain slice electrophysiology system.

It enables simultaneous extracellular stimulation, intracellular current injection, whole-cell patch-clamp recordings, and extracellular recordings from multiple sites within 50-120 µm of the soma (Figure 1a). ES effects are assessed in brain slices at the single compartment (soma) and membrane level, *i.e.*, on the extracellular ($V_e$), intracellular somatic ($V_i$), and the resulting membrane voltage ($V_m$, calculated as $V_m=V_i-V_e$) in the vicinity of the whole-cell patch-clamped soma. To study the impact of ES on $V_e$, $V_i$ and $V_m$ of single neurons we first estimated the electric field and resulting $V_e$-deflection in the vicinity of the cell body from ES delivery through an extracellular pipette as a function of distance (Figure 1a-c). The highest ES amplitude (200 nA) induced a $V_e$-amplitude of 1.1±0.5 mV (mean ± std) and a field amplitude of 22.6±8.9mV/mm (mean ± std) close to the cell body (measured 15 µm from the soma). The $V_e$-distance relationship was accurately captured by the point-source approximation for a purely resistive and homogeneous medium [19,33]. We conclude that the ES amplitudes imposed in our study are relatively weak and within the physiological range measured in rodents and humans *in vivo* (*e.g.* [16,34]).

We used acute slices of mouse primary visual cortex (V1) to focus on excitatory pyramidal cells and the two largest GABAergic cell classes in cortical layer 5 (L5), the parvalbumin (Pvalb), and somatostatin (SST)-expressing cells comprising approximately 54% and 25% of the Layer 5 GABAergic cell population, respectively [35](Figure 1d). We used several modalities (fluorescent markers in transgenic animals, electrophysiological features, and cellular morphology) to identify individual neurons from the three cell classes (Figure 1d). Specifically, excitatory pyramidal neurons were initially identified in Cre- or Flp-dependent transgenic mice (driven by L5-specific Tlx3 or Sim1 promoters) with fluorescent reporters for L5 excitatory neurons or by their pyramidal morphology, and then confirmed by their characteristic regular-spiking firing pattern in response to intracellularly injected current steps and slower F-I curve in patch-clamp recordings (e.g. [36]). Inhibitory Pvalb and SST neurons were identified using Cre- or Flp-dependent transgenic mice with fluorescent reporters and confirmed by their fast-spiking firing pattern and steep F-I curve (Figure 1d) [36]. The recorded cells were filled with biocytin, for *post-hoc* processing to reveal their cellular morphology and confirm the classification.

In principle, even weak ES can impact the cellular membrane (e.g. [19]) but whether and how it does so for different cell classes remains speculative. To address this question, we stimulated (via intracellular DC current injection) and recorded from pyramidal, Pvalb, and SST neurons while delivering ES through an extracellular stimulating electrode placed 50 µm away from the cell body. Intracellular current injections 1-2X above rheobase were used to elicit spiking during control and ES (Table S1; 154.5 ± 64.9 pA for pyramidal neurons; 259.5 ± 99.8 pA for Pvalb; 191.5 ± 102.8 pA for SST). The ES was delivered as a sinusoidal current at amplitudes from 25 to 200 nA. Such weak ES (Figure 1a-c) cannot elicit action potentials in the absence of other inputs [18,19]. We confirmed this observation independently in our setup, when extracellular ES alone was imposed at the maximum ES amplitude no change in spike frequency was observed in any of our experiments (Figure S1). The ES frequency was varied from 8 to 140 Hz covering a range used in ES applications (Figure 1e). We then mapped the spikes during sinusoidal ES to their respective spike phase along the sinusoidal ES (reference signal: $V_e$; Figure 1f). In a second step, spike-field entrainment of the different cell classes was assessed via population vector analysis (Figure 1g) (see also Methods). A strong effect of ES on neural spiking (increased spike-field entrainment) results in an inhomogeneous spike phase distribution

with a distinct, preferred spike phase and a larger population vector. Weak ES effect on neural spike timing or decreased entrainment, in turn, is marked by a homogeneous spike phase distribution and a small population vector length (e.g., control experiments where no ES is delivered; Figure 1g). We found a diversity in the entrainment profile of cortical cell classes that depends on ES parameters as well as cell class properties and activity (Figure 1g).

**Rich, diverse and cell class-specific spike-field entrainment to ES**

To understand the origin of diverse electric field entrainment we first looked at the influence of ES on the spiking cellular membrane. Hitherto the assumption has been that ES has the same effect on the neural membrane across the various classes as long as experimental parameters (e.g., distance of the ES electrode, the induced field, etc.) are controlled for. To test this hypothesis, we conducted a set of experiments where we analyzed the spiking activity of cells in the presence vs. absence of ES. To isolate the pure ES effect from effects mediated from other neurons, experiments were conducted under synaptic blockers (see Methods). To elicit spiking, we injected intracellular DC current into the cell body of neurons (intracellular stimulation duration: 9 s). This was repeated under two conditions: in the absence of any ES ("control") and, in a next step, the same intracellular current was injected while concurrently applying ES at various frequencies ($f_{stim}$ = 8, 30, 140 Hz) and amplitudes (25 to 200 nA) (Figure 2a).

To what extent does ES impact spiking? Notably, the presence or absence of ES did not alter the spike frequency elicited by the intracellular DC injection for all cell classes tested (Figure S1). Therefore, comparatively weak ES as in our experiments does not alter overall spike rate of individual cells. We next tested whether ES affected the temporal patterning of spikes: does ES give rise to temporal windows of increased or decreased spike entrainment? Because the imposed ES as well as the recorded $V_e$ in the proximity of the recorded cells is sinusoidal, spike times can be mapped to spike phases (Figure 1e-f; reference signal: $V_e$ from the electrode closest to the recorded neuron; spike phase: 0º – 360º). To test whether ES altered the temporal patterning of spike times we looked for an emerging inhomogeneity in the spike phase distribution as function of cell class and ES parameters. To control for spurious correlations, we devised the following control experiment: adopt the $V_e$-signal from the subsequent experiment where ES is present (i.e., ES amplitude is non-zero), map spike times to spike phases and run the same statistical tests for this "virtual" ES experiment. Under such conditions, a time-locked but ES-independent mechanism at any of the tested ES frequencies will result in an inhomogeneous spike-phase distribution even under control conditions. To assess whether the spike-phase distribution exhibits statistically significant inhomogeneity we used circular statistics[19,21]. Specifically, the population vector length (range 0-1) and the Rayleigh test (null hypothesis: spike-phases along the unit circle are uniformly distributed exhibiting no preferred phase) serve as a metric of spike phase coordination. The lack of spike-phase coordination results in a homogeneous spike-phase distribution, a small vector length and a statistically insignificant *p*-value of the Rayleigh test. In contrast, the presence of spike-phase coordination due to ES gives rise to an inhomogeneous spike-phase distribution (with spike-phases mapped based on the local $V_e$ signal dominated by the ES), a large vector length, and a statistically significant *p*-value of the Rayleigh test.

We first looked at pyramidal neurons where is it known that longer DC current injections lead to temporally irregular spiking [19,39]. We saw that, indeed, for control experiments, homogeneous spike-phase distributions appear with very small vector lengths, i.e., no preference is observed in terms of spike-phase in the absence of ES (Figure 2b-c, Table S2). When we incrementally increased the ES amplitude we saw the spike-phase entrainment appear as seen in the decreasing *p*-value (calculated by the Rayleigh test) and increasing vector length (Figure 2c-e, ES amplitude: 200 nA; Figure S2, ES amplitude: 100 nA, Table S2). Importantly, while spike phase distribution changed with ES, the spike frequency remained unaltered (Figure S1). We note that even at the lowest ES amplitude, i.e., 25 nA that results in a field strength of approx. 1-2 mV/mm and a $V_e$-amplitude of 0.1 mV, leads to strong spike-field coordination across frequencies for excitatory and inhibitory classes (Figure S3). It follows that weak, subthreshold ES results in strong pyramidal spike-phase coordination despite leaving the spike rate unaffected. Analysis of the pyramidal spike-phase coordination further reveals that spike-field entrainment of pyramidal neurons is ubiquitous and reaches very high ES frequencies. Specifically, while Pyr exhibit a preferred spike-field entrainment at 8 Hz ES, the same pyramidal neurons also exhibit strong spike-field coordination at very high ES frequencies (140 Hz; Figure 2b-c). We conclude that weak, subthreshold ES results in strong pyramidal spike-phase coordination and that the entrainment remains strong even for fast ES frequencies in excess of 100 Hz.

We next looked at the spike-field entrainment of major cortical inhibitory cell classes. We ran similar suprathreshold experiments (control vs. ES) with Pvalb and SST inhibitory cells and performed identical analyses calculating the same entrainment metrics. In sharp contrast to pyramidal neurons, we found that both Pvalb and SST entrain their spiking predominantly to high ES frequencies: SST entrain for >30 Hz whereas Pvalb exhibit strong spike-field coordination for 140 Hz and much weaker coordination for slower ES of the same amplitude (Figure 2c-e, Table S2). Once more, the spike-field entrainment observed in Pvalb and SST is solely attributed to the impact of ES: control experiments where ES is absent (zero amplitude) show no coordination between spiking and any effect in a similar time scale to ES for any cell class. It is only when weak ES is imposed at the right frequency for each inhibitory class that Pvalb and SST spiking is entrained (e.g., compare Pvalb spike-phase distributions for 8 and 30 Hz; Figure 2b; Figure S2, S4).We conclude that while Pvalb and SST inhibitory neurons exhibit strong spike-field entrainment to ES, this entrainment depends on the ES parameters with cells exhibiting a particular preference to fast ES (>30 Hz for SST and 140 Hz for Pvalb).

Surprised by the richness of the spike-field entrainment characteristics, we sought to reproduce our basic findings in another brain region. We repeated our experimental protocols in the hippocampus, recording from pyramidal neurons and Pvalb located in the CA1. We used the same ES protocols as in V1, which we found produced very similar field strengths (Figure S5a-c). As for V1 neurons, we found that subthreshold entrainment characteristics are very similar between the excitatory and inhibitory CA1 cell classes (Figure S5d-e). When we looked at the suprathreshold, spiking entrainment of CA1 neurons to ES we found that our basic findings hold: weak, subthreshold ES results in strong pyramidal spike-phase coordination with increasing ES amplitude resulting in increasing spike-field entrainment that remains strong even for fast ES frequencies (> 100 Hz;  Figure S5f-i; S6). Hippocampal inhibitory Pvalb on the other hand, like their V1 counterparts, exhibit a much more nonlinear spike-field entrainment profile with a clear preference to fast ES (Figure S5f-i, S6, Table S3). We conclude that the rich and diverse spike-

field entrainment characteristics to ES shown in V1 are also observed in hippocampal CA1 strongly indicating that our findings are robust and resulting from a fundamental biophysical mechanism shared across cortical areas.

**Ubiquitous and robust subthreshold entrainment across cell classes**

Given the strong and class-specific entrainment of spiking to ES, we asked how this effect is mediated. Specifically, we asked whether ES also impacts the non-spiking (subthreshold) membrane in a differential, class-specific manner that then results in the observed spike entrainment. To do so we looked at pyramidal, Pvalb, and SST neurons in two regimes: first, by holding the cells at their resting potential (Table S1) and, second, by holding them at various subthreshold polarization levels. Under both conditions, we delivered sinusoidal ES of varying amplitude (25-200 nA) and frequency (1-100 Hz) delivered 50 µm from cell soma. To assess the effects of ES on the subthreshold neurons, we analyzed the resulting amplitude and phase deflections of $V_e$, $V_i$, and $V_m$ (Figure 3).

In the presence of synaptic blockers (see Methods) and absence of intracellular current injection, the $V_e$, $V_i$, and $V_m$ response (amplitude and phase) to ES measures the pure subthreshold ES effect on the cellular membrane (Figure 3a-c). We found that all cell classes readily entrain to the sinusoidal ES, irrespective of ES amplitude and frequency (Figure 3a; N=24 pyramidal, 22 Pvalb, 13 SST cells). Specifically, ES induced a local $V_e$ oscillation (measured from the closest extracellular electrode at 15 µm from the soma) that remained unaltered in amplitude (Figure 3b) and phase (Figure 3c) for 1-100 Hz. When looking at $V_i$ and $V_m$ (as estimated by the difference between $V_i$ and $V_e$) we found that the intracellular and the membrane potential at the soma of all cell classes followed all tested ES frequencies up to 100 Hz without any sign of membrane filtering (Figure 3b-c). Our findings are consistent with AC electrodynamics theory predicting that the cell membrane voltage polarization induced by an external ES drive remains constant even for very high frequencies (e.g. [37,38] ). It follows that ES presents a fundamentally different stimulus compared to intracellular stimulation where membrane RC filtering greatly attenuates higher frequencies and allows lower frequencies to shape the membrane response. We also note that the amplitude of the pure ES effect induced in all cell classes was a fraction of 1 mV ($V_m$ amplitude: 0.29±0.26mV, Pyr; 0.36±0.23 mV, Pvalb; 0.34±0.11 mV, SST; Figure 3b). We conclude that all cells in the excitatory and inhibitory cell classes entrain to subthreshold ES unperturbed, from low to high frequencies (up to 100 Hz), without any apparent filtering while the ES impact on the cellular membrane remains relatively modest in amplitude.

To what extent is such small but unimpeded membrane entrainment across cell classes a result of the membrane residing at rest? To address this question, we depolarized and hyperpolarized all cells relative to their resting potential via intracellular DC injections and assessed the impact of ES on $V_e$, $V_i$ and $V_m$ (Figure 3d-f). Simultaneous to the ES delivery we also delivered intracellular current DC injections (from -90 pA to 60 pA, duration: 5 s) to induce subthreshold-level changes in membrane polarization. The concurrent ES was set at 100 nA at 8Hz. We found that, once more, the subthreshold, ES-induced effect remained robust and unchanged across cell classes in terms of the $V_i$ and $V_m$-amplitude and -phase even when the membrane polarization was varied by 40-50 mV (Figure 3d-f). In summary, we find that at

subthreshold, rest and polarized levels, the cell membrane can follow the applied ES and does so robustly across all cell classes.

**Spike-field entrainment strongly correlates with spike frequency of the cell**

While cortical classes show strong, class-specific spike entrainment to ES, the same neurons exhibit indistinguishable entrainment characteristics to the same sinusoidal ES when not spiking: pyramidal neurons exhibit a combination of non-specific and frequency-specific (8 and 140 Hz) spike-field entrainment, inhibitory Pvalb neurons only entrain to high frequencies (140 Hz) while inhibitory SST entrains to medium-to-high frequencies (> 30 Hz). How are these observations reconciled? To investigate whether cellular properties can explain ES entrainment we looked at four intrinsic properties – spike threshold, firing rate, input resistance and resting voltage [36]. Looking at the intrinsic properties vs. the resulting spike-field strength (expressed by the vector length) we found that intrinsic cellular properties do not explain within-class ES entrainment (Figure S7). With respect to between-class differences, intrinsic properties in the absence of ES do not result in any ES entrainment (see phase-distributions of control experiments). Therefore, ES is paramount for the emergence of spike-field entrainment even in the presence of differential intrinsic properties between classes. We conclude that the stereotypical intrinsic properties do not explain the strong frequency-dependence seen in the spike-field coordination of the three cortical classes.

We next looked at the temporal structure of spiking for mechanisms that explain the ES frequency-dependence. To do so we calculated the interspike interval (ISI) for each spike (Figure 4a). Consistent with other studies [36], the ISI distributions show the stereotypical slow and irregular firing pyramidal neurons are known for (spike rate: 8.5±3.0 Hz) as well as the fast, more stereotyped firing of Pvalb (133.4±35.7 Hz; Figure 4b). Finally, SST present an intermediate and more diverse case with faster spike rate than Pyr though slower than Pvalb and with a considerably wider ISI-distribution (57.4±37.8 Hz; Figure 4b). Closer examination of the entrainment analysis suggests that at least a portion of the highly entrained spikes stem from neurons spiking at similar frequencies to the ES frequency, implying that for a given spike j, when (ES frequency) ≈ 1/ISI_j , the coordination between sinusoidal ES and spike j is enhanced. To test this hypothesis, we separated spikes based on whether their ISI was within a certain window of the ES frequency. For example, we looked at the spike-field coherence of pyramidal neurons with a spike frequency (1/ISI) of 8 Hz ("center frequency") ± (frequency window) when the ES frequency is also 8 Hz (Figure 4c). We then varied the frequency window width and looked at whether the resulting population vector length changed within each bin. If no measurable difference is observed in terms of the vector length, then entrainment occurs equally strong across spike rate bins with no preference (in terms of ISI). If, on the other hand, spikes whose inverse ISI is close to the ES frequency are strongly entrained compared to the rest, then this supports a resonance-like mechanism where subpopulations of neurons are candidates to be highly entrained to a particular ES frequency depending on their ISI. The results from pyramidal neurons exhibit evidence for both phenomena (Figure 4c-d). While a subset of spikes (with 1/ISI ≈ ES frequency) are strongly entrained to the ES compared to the rest (Figure 4d), there is still substantial entrainment across pyramidal neurons (compared to control) and especially to ES frequencies much higher than pyramidal 1/ISI.

To what extent do such highly entrained subpopulations of spikes exist in other cell classes? We used the same principle to look at spike-field entrainment as function of ISI by varying the window (width) around the center frequency (see also Methods). The main difference between Pvalb and SST compared to pyramidal neurons is their discrepancy in spike rate (Figure 4b). For Pvalb, the condition 1/ISI ≈ ES frequency can only be met for ES frequency 140 Hz since Pvalb typically spike around 100-200 Hz. For SST the same condition holds for ES frequency around 30 Hz since they tend to spike around 20-100 Hz (Figure 4b). Spike-field entrainment of spikes at various ES frequencies is significantly increased when 1/ISI ≈ ES frequency across cell classes (Figure 4d-e). While this principle holds in general, the specifics of the entrainment profile differ between cell classes. For example, for pyramidal neurons at 8 Hz, spikes where 1/ISI deviates from the ES frequency by approx. 20%, exhibit a decrease in their degree of entrainment (vector length) by more than 50% (Figure 4e). On the other hand, for Pvalb at 140 Hz, 1/ISI can deviate by more than 35% (1/ISI≈90 Hz) without spikes experiencing an appreciable decrease in their entrainment. Finally, SST at 30 Hz form an intermediate case where spikes off by approx. 33% (1/ISI≈21 Hz) still exhibit 50-75% of the entrainment (Figure 4e). These observations are compatible with what is known about the cell classes explored in our study. Despite the entrainment of pyramidal neurons to subthreshold frequencies across ES frequencies, their irregular spiking due to a plethora of active and co-activated membrane mechanisms is a constant source of variability counteracting field entrainment that results in a tight entrainment window around the center frequency. On the other hand, once Pvalb with their fast and less adaptive spike-related mechanisms are entrained, there is little source of variability to counteract field entrainment which, in turn, results in a wide entrainment window around the center frequency. We conclude that class-specific spike-field coordination is the result of two effects: first, a non-specific membrane polarization ubiquitously present across cells and classes; second, class-specific excitability and activity properties that allow spikes of similar time scale to the ES to entrain particularly strongly. The latter effect is class-specific since how steeply spike-field entrainment drops for spikes where 1/ISI deviates from ES frequency varies across classes.

**Spike-field entrainment of human neocortical excitatory neurons to ES**

To what extent are the ES effects seen in rodent V1 and validated in hippocampal CA1 also translated to human? While human pyramidal neurons share properties with their rodent counterparts (e.g. [40,41] ), they also possess many distinct characteristics (e.g. [42,43] ). The latter will also impact the entrainment characteristics of human neurons to ES. This, in turn, could affect how human vs. rodent neurons should get stimulated to achieve a certain activity pattern. We used our setup to investigate the subthreshold and spiking ES effects of human cortical (temporal or frontal lobe) neurons isolated from neurosurgical specimens [44].

We imposed the same, relatively weak sinusoidal ES field across human pyramidal neurons and measured how $V_e$, $V_i$ and $V_m$ are affected by the ES strength and frequency (Figure 5a; field strength similar to rodent slices, compare Figure 5b to 2b) under two regimes spiking (Figure 5c-e) and subthreshold non-spiking (Figure 5f). For subthreshold ES we found that human pyramidal cells in entrain to subthreshold ES unperturbed, from low to high frequencies (up to 100 Hz), without any apparent filtering. Also, we found that at subthreshold, rest and polarized levels, the human cell membrane readily follows the applied ES across polarization levels robustly (Figure 5f).

How about ES entrainment under spiking conditions? Like for rodent neurons, we injected intracellular DC stimuli to elicit spiking simultaneously to the ES application. ES did not affect the spike rate of human neurons (paired *t*-test, $p > 0.05$ for control vs. 8 Hz, 30 Hz, and 140 Hz for all amplitudes tested) validating that, compared to the intracellular stimulation, the impact of ES on the membrane is comparatively weak. Moreover, in the absence of ES (control), spikes do not exhibit any entrainment at the frequencies related to ES (Rayleigh testing, $p>0.1$; Figure 5g-k). It is only in the presence of ES that spike-field entrainment occurs with increases in ES amplitude resulting in increased spike-field coordination (Figure 5g-k). Uniquely, human pyramidal neurons exhibit the strongest spike-field entrainment for high ES frequencies (140 Hz) despite their slower spiking (spike rate: 7.5±0.8 Hz). We also looked at the extent to which spikes with 1/ISI ≈ (ES frequency) entrain more strongly than the rest (Figure 5l-m). Given the slow spiking of human pyramidal neurons, this condition can only be satisfied for 8 Hz. We found that for 8 Hz, an ES frequency that human neurons entrain readily to, spikes with 1/ISI≈8 Hz entrain particularly strongly compared to spikes with a more disparate spike frequency, with inclusion of such spikes resulting in the quick deterioration of coordination (Figure 5l-m). Thus, also for human excitatory neurons, there is a subset of highly coordinated spikes where 1/ISI≈8 Hz. On the other hand, the very high entrainment of human excitatory spiking with fast ES frequencies, much faster than any spiking, and the subthreshold entrainment properties of their membrane to fast stimuli also point to a mechanism very similar to the non-specific membrane polarization observed in rodent neurons. Similar trends are also observed even for weaker ES amplitudes (Figure S8). We conclude that, similar as in rodent neurons, spike-field coordination in human excitatory neurons is a combination of two effects: non-specific membrane polarization ubiquitously present across cells and a spike activity-related effect that allows spikes of similar time scale to the ES to entrain particularly strongly.

## Discussion

We found that membrane entrainment to a relatively weak (in amplitude) sinusoidal ES occurs across all cell classes (excitatory and inhibitory), multiple cortical areas (V1 and hippocampus) and, in fact, species (rodent and human) pointing to a fundamental property of single neurons. While intracellular current injections generally result in strong membrane filtering (i.e., higher frequencies are greatly attenuated), membrane response to extracellular ES remains essentially unfiltered even for frequencies where intracellular stimuli do not survive (for frequencies >100 Hz; [45] ). This is a generic property shared across all neurons and classes in our study. Yet, this generic property gives rise to rich and diverse class-specific spike-field coordination in the presence of ES. Specifically, we found that pyramidal neurons with their typically slower spike rate entrain to slow and fast ES while inhibitory classes like Pvalb and SST with their comparatively fast spiking predominantly phase lock to fast ES. A resonant mechanism that purely relies on a match between spike rate and ES frequency explains pyramidal coupling to 8 Hz ES as well as Pvalb coupling to 140 Hz but cannot explain the pyramidal and, to a lesser extent, SST coupling to very fast ES in our experiments. We note that the class-specific spike-field coordination stems from the use of sinusoidal ES rather than alternative waveforms (e.g., pulses) where the fundamental frequency of the stimulus is obscured, and the response occurs at multiple time scales. We conclude that sinusoidal ES entrains subthreshold and spiking activity across cell classes resulting in a rich repertoire of their suprathreshold response.

Our experiments point to class-specific spike-field coordination being the result of two effects: non-specific membrane polarization ubiquitously present across cells and classes and class-specific excitability and spike activity properties eliciting spikes at similar time scales to the ES that strongly entrain. The spike profile of the classes we examined is as diverse as the conductances expressed on these cells with some of them also linked to subthreshold resonant and ES effects like the m-current [46,47], the hyperpolarization-activated cation current Ih [41,48] for pyramidal neurons. The characteristic spike profile is a result of the interaction between the unique ionic setup and morphology properties. Even so, we found that distinct cortical classes with vastly different spiking profiles across brain areas and species exhibit ubiquitous and robust coordination to ES in a spectrum of frequencies. This observation suggests that membrane entrainment is a fundamental property not mediated by a specific ion conductance (though the presence of specific conductances can increase or decrease coupling properties, e.g. [46,47]). Yet, since how a cell spikes (from its spike waveform to the excitability profile and its resulting spike rate) is crucially affected by its ionic setup, the distinct ionic setup of each class is implicitly reflected in the properties of ES entrainment. For example, while V1 pyramidal neurons typically spike slowly, their spike rate can increase drastically during bursting (i.e., 200-300 Hz) mediated by a host of somadendritic mechanisms suggesting that their ionic setup, in principle, supports fast activity and locking to fast ES [49–54]. We conclude that while ES entrainment is ubiquitous, the characteristics of spike-field entrainment for each cortical class ultimately reflects its morphoelectric properties and ionic setup.

Our findings shed light to cellular ES effects and are relevant for several applications like the design of next-generation neuromodulation technologies using customized ES waveforms for the selective coordination of specific cell classes *in vivo*. The main parameter exerting such selectivity based on our results is the ES frequency with slow ES facilitating coordination between excitatory classes while fast ES facilitates excitatory and inhibitory coordination. Spike-field coordination in various frequency bands is the substrate of many cognitive functions and therapeutic interventions [34,55–57]. Beyond local ES effects in the vicinity of the stimulation site, class-specific ES protocols can impact spatially distributed brain regions away from the stimulation site. For example, in humans, cortical structures have reliable monosynaptic connections to the subthalamic nucleus (STN), an area with a diverse functional role and a major target for deep brain stimulation, e.g. in movement disorders [4,6,58–62]. Class-specific stimulation of cortex via ES may allow the selective neuromodulation of individual STN classes based on their projection pattern and, in such manner, alter behavior or facilitate therapy. Our findings form the basis for designing such selective, class-specific ES interventions in the local circuit as well as in the projection areas of the locally entrained cell classes.

Coordinated circuit activity often produces a measurable extracellular field, especially so in cortical structures like the hippocampus and neocortex [63]. Because the field strength in our experiments is comparable to what is measured *in vivo*, our results can shed light in cellular entrainment when the field is generated from purely endogenous processing (so-called ephaptic coupling [64]). The ubiquitous nature of ES coupling suggests that slower (e.g., alpha, theta, beta) and faster endogenous oscillations (gamma, ripples) are felt and followed by the membrane across cortical neurons. To what extent is spiking affected by such oscillations in a manner that constitutes an alternative, non-synaptic communication between neurons? In the absence of

synaptic drive that sufficiently depolarizes neurons and leads to spiking, endogenous fields are rarely strong enough to elicit it under physiological conditions. But, in the presence of such synaptic drive (that often results in a strong extracellular field, [63]), electric fields can strongly affect spike timing. For example, Purkinje cells in the cerebellum coordinate their spiking with ms precision through ephaptic coupling [26]. Fast coordination (within ms) between pyramidal neurons has also also observed in neocortex (e.g. [52]) with synapses there only supporting slower coordination. The spike-field coupling we see across classes for fast ES (140 Hz) can explain such fast coordination even in the absence of very fast synapses and, in such manner, provide an alternative, energy-efficient non-synaptic paradigm for circuit coordination across timescales in cortical structures.

## References


1. Hitzig, E. (1874). Untersuchungen über das Gehirn: Abhandlungen physiologischen und pathologischen Inhalts (A. Hirschwald).

2. Fritsch, G. (1870). Uber die elektrische Erregbarkeit des Grosshirns. Arch, anat. Physiol. Wiss. Med. *37*, 300–332.

3. Dumitrascu, O.M., Kamiński, J., Rutishauser, U., and Tagliati, M. (2016). Subthalamic Nuclei Deep Brain Stimulation Improves Color Vision in Patients with Parkinson's Disease. Brain Stimulation: Basic, Translational, and Clinical Research in Neuromodulation *9*, 948–949. 10.1016/j.brs.2016.08.006.

4. Vitek, J.L., Jain, R., Chen, L., Tröster, A.I., Schrock, L.E., House, P.A., Giroux, M.L., Hebb, A.O., Farris, S.M., Whiting, D.M., et al. (2020). Subthalamic nucleus deep brain stimulation with a multiple independent constant current-controlled device in Parkinson's disease (INTREPID): a multicentre, double-blind, randomised, sham-controlled study. The Lancet Neurology *19*, 491–501. 10.1016/S1474-4422(20)30108-3.

5. Freund H, Kuhn J, Lenartz D, and et al (2009). COgnitive functions in a patient with parkinson-dementia syndrome undergoing deep brain stimulation. Arch Neurol *66*, 781–785. 10.1001/archneurol.2009.102.

6. Hogg, E., During, E., E. Tan, E., Athreya, K., Eskenazi, J., Wertheimer, J., Mamelak, A.N., Alterman, R.L., and Tagliati, M. (2018). Sustained quality-of-life improvements over 10 years after deep brain stimulation for dystonia. Movement Disorders *33*, 1160–1167. 10.1002/mds.27426.

7. Mayberg, H.S., Lozano, A.M., Voon, V., McNeely, H.E., Seminowicz, D., Hamani, C., Schwalb, J.M., and Kennedy, S.H. (2005). Deep Brain Stimulation for Treatment-Resistant Depression. Neuron *45*, 651–660. 10.1016/j.neuron.2005.02.014.

8. Lozano, A.M., Mayberg, H.S., Giacobbe, P., Hamani, C., Craddock, R.C., and Kennedy, S.H. (2008). Subcallosal cingulate gyrus deep brain stimulation for treatment-resistant depression. Biol. Psychiatry *64*, 461–467. 10.1016/j.biopsych.2008.05.034.

9. Holtzheimer, P.E., Kelley, M.E., Gross, R.E., Filkowski, M.M., Garlow, S.J., Barrocas, A., Wint, D., Craighead, M.C., Kozarsky, J., Chismar, R., et al. (2012). Subcallosal cingulate deep brain stimulation for treatment-resistant unipolar and bipolar depression. Arch. Gen. Psychiatry *69*, 150–158. 10.1001/archgenpsychiatry.2011.1456.

10. Vonck, K., Boon, P., Achten, E., De Reuck, J., and Caemaert, J. (2002). Long-term amygdalohippocampal stimulation for refractory temporal lobe epilepsy. Annals of Neurology *52*, 556–565. 10.1002/ana.10323.

11. Hodaie, M., Wennberg, R.A., Dostrovsky, J.O., and Lozano, A.M. (2002). Chronic Anterior Thalamus Stimulation for Intractable Epilepsy. Epilepsia *43*, 603–608. 10.1046/j.1528-1157.2002.26001.x.

12. Kringelbach, M.L., Jenkinson, N., Owen, S.L.F., and Aziz, T.Z. (2007). Translational principles of deep brain stimulation. Nat. Rev. Neurosci. *8*, 623–635. 10.1038/nrn2196.

13. Arvanitaki, A. (1942). Effects evoked in an axon by the activity of a contiguous one. Journal of Neurophysiology *5*, 89–108. 10.1152/jn.1942.5.2.89.

14. Arvanitaki, A., and Chalazonitis, N. (1947). De La Nature Des laquoPotentiels D'Activitéraquo II. — Initiation De L'Activité Oscillatoire Neuronique Par Des Anions Aptes A Se Coordonner Avec Les Métaux Des Catalyseurs Respiratoires. Archives Internationales de Physiologie *54*, 423–440. 10.3109/13813454709144832.

15. Holt, G.R., and Koch, C. (1999). Electrical interactions via the extracellular potential near cell bodies. J Comput Neurosci *6*, 169–184.

16. Anastassiou, C.A., Montgomery, S.M., Barahona, M., Buzsáki, G., and Koch, C. (2010). The effect of spatially inhomogeneous extracellular electric fields on neurons. J. Neurosci. *30*, 1925–1936. 10.1523/JNEUROSCI.3635-09.2010.

17. Aspart, F., Remme, M.W.H., and Obermayer, K. (2018). Differential polarization of cortical pyramidal neuron dendrites through weak extracellular fields. PLOS Computational Biology *14*, e1006124. 10.1371/journal.pcbi.1006124.

18. Histed, M.H., Bonin, V., and Reid, R.C. (2009). Direct Activation of Sparse, Distributed Populations of Cortical Neurons by Electrical Microstimulation. Neuron *63*, 508–522. 10.1016/j.neuron.2009.07.016.

19. Anastassiou, C.A., Perin, R., Markram, H., and Koch, C. (2011). Ephaptic coupling of cortical neurons. Nat Neurosci *14*, 217–223. 10.1038/nn.2727.

20. Deans, J.K., Powell, A.D., and Jefferys, J.G. (2007). Sensitivity of coherent oscillations in rat hippocampus to AC electric fields. The Journal of physiology *583*, 555–565.

21. Radman, T., Su, Y., An, J.H., Parra, L.C., and Bikson, M. (2007). Spike timing amplifies the effect of electric fields on neurons: implications for endogenous field effects. J. Neurosci. *27*, 3030–3036. 10.1523/JNEUROSCI.0095-07.2007.

22. Reato, D., Rahman, A., Bikson, M., and Parra, L.C. (2010). Low-intensity electrical stimulation affects network dynamics by modulating population rate and spike timing. The Journal of Neuroscience *30*, 15067–15079.

23. Chiang, C.-C., Shivacharan, R.S., Wei, X., Gonzalez-Reyes, L.E., and Durand, D.M. (2019). Slow periodic activity in the longitudinal hippocampal slice can self-propagate non-synaptically by a mechanism consistent with ephaptic coupling. The Journal of physiology *597*, 249–269.

24. Chan, C.Y., and Nicholson, C. (1986). Modulation by applied electric fields of Purkinje and stellate cell activity in the isolated turtle cerebellum. The Journal of physiology *371*, 89–114.

25. Freeman, D.K., Eddington, D.K., Rizzo, J.F., and Fried, S.I. (2010). Selective Activation of Neuronal Targets With Sinusoidal Electric Stimulation. Journal of Neurophysiology *104*, 2778–2791. 10.1152/jn.00551.2010.

26. Han, K.-S., Guo, C., Chen, C.H., Witter, L., Osorno, T., and Regehr, W.G. (2018). Ephaptic coupling promotes synchronous firing of cerebellar purkinje cells. Neuron *100*, 564–578.

27. Freund, T. f., and Buzsáki, G. (1996). Interneurons of the hippocampus. Hippocampus *6*, 347–470. 10.1002/(SICI)1098-1063(1996)6:4<347::AID-HIPO1>3.0.CO;2-I.

28. Petilla terminology: nomenclature of features of GABAergic interneurons of the cerebral cortex (2008). Nat Rev Neurosci *9*, 557–568. 10.1038/nrn2402.

29. Tremblay, R., Lee, S., and Rudy, B. (2016). GABAergic Interneurons in the Neocortex: From Cellular Properties to Circuits. Neuron *91*, 260–292. 10.1016/j.neuron.2016.06.033.

30. Stark, E., Eichler, R., Roux, L., Fujisawa, S., Rotstein, H.G., and Buzsáki, G. (2013). Inhibition-Induced Theta Resonance in Cortical Circuits. Neuron *80*, 1263–1276. 10.1016/j.neuron.2013.09.033.

31. Stark, E., Roux, L., Eichler, R., Senzai, Y., Royer, S., and Buzsáki, G. (2014). Pyramidal Cell-Interneuron Interactions Underlie Hippocampal Ripple Oscillations. Neuron *83*, 467–480. 10.1016/j.neuron.2014.06.023.

32. Radman, T., Ramos, R.L., Brumberg, J.C., and Bikson, M. (2009). Role of cortical cell type and morphology in subthreshold and suprathreshold uniform electric field stimulation in vitro. Brain Stimulation *2*, 215-228.e3. 10.1016/j.brs.2009.03.007.

33. Anastassiou, C.A., Perin, R., Buzsáki, G., Markram, H., and Koch, C. (2015). Cell type- and activity-dependent extracellular correlates of intracellular spiking. J. Neurophysiol. *114*, 608–623. 10.1152/jn.00628.2014.

34. Rutishauser, U., Ross, I.B., Mamelak, A.N., and Schuman, E.M. (2010). Human memory strength is predicted by theta-frequency phase-locking of single neurons. Nature *464*, 903–907. 10.1038/nature08860.

35. Xu, X., Roby, K.D., and Callaway, E.M. (2010). Immunochemical characterization of inhibitory mouse cortical neurons: Three chemically distinct classes of inhibitory cells. J. Comp. Neurol. *518*, 389–404. 10.1002/cne.22229.

36. Gouwens, N.W., Sorensen, S.A., Berg, J., Lee, C., Jarsky, T., Ting, J., Sunkin, S.M., Feng, D., Anastassiou, C.A., Barkan, E., et al. (2019). Classification of electrophysiological and morphological neuron types in the mouse visual cortex. Nature Neuroscience *22*, 1182–1195. 10.1038/s41593-019-0417-0.

37. Gimsa, J., and Wachner, D. (2001). Analytical description of the transmembrane voltage induced on arbitrarily oriented ellipsoidal and cylindrical cells. Biophys J *81*, 1888–1896.

38. Maswiwat, K., Wachner, D., Warnke, R., and Gimsa, J. (2007). Simplified equations for the transmembrane potential induced in ellipsoidal cells of rotational symmetry. J. Phys. D: Appl. Phys. *40*, 914. 10.1088/0022-3727/40/3/033.

39. Mainen, Z.F., and Sejnowski, T.J. (1995). Reliability of spike timing in neocortical neurons. Science *268*, 1503–1506.

40. Berg, J., Sorensen, S.A., Ting, J.T., Miller, J.A., Chartrand, T., Buchin, A., Bakken, T.E., Budzillo, A., Dee, N., Ding, S.-L., et al. (2021). Human neocortical expansion involves glutamatergic neuron diversification. Nature *598*, 151–158. 10.1038/s41586-021-03813-8.

41. Kalmbach, B.E., Buchin, A., Long, B., Close, J., Nandi, A., Miller, J.A., Bakken, T.E., Hodge, R.D., Chong, P., de Frates, R., et al. (2018). h-Channels Contribute to Divergent Intrinsic Membrane Properties of Supragranular Pyramidal Neurons in Human versus Mouse Cerebral Cortex. Neuron *100*, 1194-1208.e5. 10.1016/j.neuron.2018.10.012.

42. Eyal, G., Verhoog, M.B., Testa-Silva, G., Deitcher, Y., Lodder, J.C., Benavides-Piccione, R., Morales, J., DeFelipe, J., de Kock, C.P., Mansvelder, H.D., et al. Unique membrane properties and enhanced signal processing in human neocortical neurons. eLife *5*. 10.7554/eLife.16553.

43. Beaulieu-Laroche, L., Toloza, E.H., Van der Goes, M.-S., Lafourcade, M., Barnagian, D., Williams, Z.M., Eskandar, E.N., Frosch, M.P., Cash, S.S., and Harnett, M.T. (2018). Enhanced dendritic compartmentalization in human cortical neurons. Cell *175*, 643–651.

44. Buchin, A., Frates, R. de, Nandi, A., Mann, R., Chong, P., Ng, L., Miller, J., Hodge, R., Kalmbach, B., Bose, S., et al. (2020). Multi-modal characterization and simulation of human epileptic circuitry. bioRxiv, 2020.04.24.060178. 10.1101/2020.04.24.060178.

45. Koch, C. (2004). Biophysics of Computation: Information Processing in Single Neurons (Oxford University Press).

46. Gutfreund, Y., Yarom, Y., and Segev, I. (1995). Subthreshold oscillations and resonant frequency in guinea-pig cortical neurons: physiology and modelling. The Journal of Physiology *483*, 621–640. 10.1113/jphysiol.1995.sp020611.

47. Hutcheon, B., and Yarom, Y. (2000). Resonance, oscillation and the intrinsic frequency preferences of neurons. Trends in Neurosciences *23*, 216–222. 10.1016/S0166-2236(00)01547-2.

48. Hutcheon, B., Miura, R.M., and Puil, E. (1996). Models of subthreshold membrane resonance in neocortical neurons. Journal of Neurophysiology *76*, 698–714. 10.1152/jn.1996.76.2.698.

49. Chagnac-Amitai, Y., Luhmann, H.J., and Prince, D.A. (1990). Burst generating and regular spiking layer 5 pyramidal neurons of rat neocortex have different morphological features. Journal of Comparative Neurology *296*, 598–613. 10.1002/cne.902960407.

50. Buzsáki, G., and Kandel, A. (1998). Somadendritic backpropagation of action potentials in cortical pyramidal cells of the awake rat. Journal of Neurophysiology *79*, 1587–1591.

51. Williams, S.R., and Stuart, G.J. (1999). Mechanisms and consequences of action potential burst firing in rat neocortical pyramidal neurons. J Physiol *521*, 467–482. 10.1111/j.1469-7793.1999.00467.x.

52. Kandel, A., and Buzsáki, G. (1997). Cellular–Synaptic Generation of Sleep Spindles, Spike-and-Wave Discharges, and Evoked Thalamocortical Responses in the Neocortex of the Rat. J. Neurosci. *17*, 6783–6797. 10.1523/JNEUROSCI.17-17-06783.1997.

53. Larkum, M.E., Nevian, T., Sandler, M., Polsky, A., and Schiller, J. (2009). Synaptic integration in tuft dendrites of layer 5 pyramidal neurons: a new unifying principle. Science *325*, 756–760.

54. Shai, A.S., Anastassiou, C.A., Larkum, M.E., and Koch, C. (2015). Physiology of Layer 5 Pyramidal Neurons in Mouse Primary Visual Cortex: Coincidence Detection through Bursting. PLoS Comput. Biol. *11*, e1004090. 10.1371/journal.pcbi.1004090.

55. Fries, P., Reynolds, J.H., Rorie, A.E., and Desimone, R. (2001). Modulation of Oscillatory Neuronal Synchronization by Selective Visual Attention. Science *291*, 1560–1563. 10.1126/science.1055465.

56. Womelsdorf, T., Fries, P., Mitra, P.P., and Desimone, R. (2006). Gamma-band synchronization in visual cortex predicts speed of change detection. Nature *439*, 733–736. 10.1038/nature04258.

57. Canolty, R.T., Edwards, E., Dalal, S.S., Soltani, M., Nagarajan, S.S., Kirsch, H.E., Berger, M.S., Barbaro, N.M., and Knight, R.T. (2006). High gamma power is phase-locked to theta oscillations in human neocortex. Science *313*, 1626–1628. 10.1126/science.1128115.

58. Mosher, C.P., Mamelak, A.N., Malekmohammadi, M., Pouratian, N., and Rutishauser, U. (2021). Distinct roles of dorsal and ventral subthalamic neurons in action selection and cancellation. Neuron *109*, 869-881.e6. 10.1016/j.neuron.2020.12.025.

59. Benabid, A.L., Pollak, P., Gross, C., Hoffmann, D., Benazzouz, A., Gao, D.M., Laurent, A., Gentil, M., and Perret, J. (1995). Acute and Long-Term Effects of Subthalamic Nucleus Stimulation in Parkinson's Disease. Stereotact Funct Neurosurg *62*, 76–84. 10.1159/000098600.

60. Brown, P., Mazzone, P., Oliviero, A., Altibrandi, M.G., Pilato, F., Tonali, P.A., and Di Lazzaro, V. (2004). Effects of stimulation of the subthalamic area on oscillatory pallidal activity in Parkinson's disease. Experimental Neurology *188*, 480–490. 10.1016/j.expneurol.2004.05.009.

61. Aron, A.R., Fletcher, P.C., Bullmore, E.T., Sahakian, B.J., and Robbins, T.W. (2003). Stop-signal inhibition disrupted by damage to right inferior frontal gyrus in humans. Nature neuroscience *6*, 115–116.

62. Aron, A.R., and Poldrack, R.A. (2006). Cortical and subcortical contributions to stop signal response inhibition: role of the subthalamic nucleus. Journal of Neuroscience *26*, 2424–2433.

63. Buzsáki, G., Anastassiou, C.A., and Koch, C. (2012). The origin of extracellular fields and currents--EEG, ECoG, LFP and spikes. Nat. Rev. Neurosci. *13*, 407–420. 10.1038/nrn3241.

64. Anastassiou, C.A., and Koch, C. (2015). Ephaptic coupling to endogenous electric field activity: why bother? Current Opinion in Neurobiology *31*, 95–103. 10.1016/j.conb.2014.09.002.

65. Allen Cell Types Database, TECHNICAL WHITE PAPER: ELECTROPHYSIOLOGY (available at: http://help.brain-map.org/display/celltypes/Documentation) (2017).

66. Campagnola, L., Seeman, S.C., Chartrand, T., Kim, L., Hoggarth, A., Gamlin, C., Ito, S., Trinh, J., Davoudian, P., Radaelli, C., et al. (2022). Local connectivity and synaptic dynamics in mouse and human neocortex. Science *375*, eabj5861. 10.1126/science.abj5861.

67. Campagnola, L., Seeman, S.C., Chartrand, T., Kim, L., Hoggarth, A., Gamlin, C., Ito, S., Trinh, J., Davoudian, P., and Radaelli, C. (2022). Local connectivity and synaptic dynamics in mouse and human neocortex. Science *375*, eabj5861.

68. Campagnola, L., Kratz, M.B., and Manis, P.B. (2014). ACQ4: an open-source software platform for data acquisition and analysis in neurophysiology research. Front. Neuroinform. *8*. 10.3389/fninf.2014.00003.

69. Kalmbach, B.E., Buchin, A., Long, B., Close, J., Nandi, A., Miller, J.A., Bakken, T.E., Hodge, R.D., Chong, P., de Frates, R., et al. (2018). h-Channels Contribute to Divergent Intrinsic Membrane Properties of Supragranular Pyramidal Neurons in Human versus Mouse Cerebral Cortex. Neuron *100*, 1194-1208.e5. 10.1016/j.neuron.2018.10.012.

70. Virtanen, P., Gommers, R., Oliphant, T.E., Haberland, M., Reddy, T., Cournapeau, D., Burovski, E., Peterson, P., Weckesser, W., Bright, J., et al. (2020). SciPy 1.0: fundamental algorithms for scientific computing in Python. Nat Methods *17*, 261–272. 10.1038/s41592-019-0686-2.

## Acknowledgments

We thank the Allen Institute Transgenic Colony Management, Tissue Processing, Histology, Imaging, Morphology and 3D reconstruction teams for their assistance in this work, and the surgeons at the University of Washington Medical Center, Swedish Medical Center and Harborview Medical Center for human tissue collection. We thank Ueli Rutishauser for discussions and suggested analyses. CAA thanks the Board of Governors of Cedars-Sinai Medical Center. Research reported in this publication was supported by the National Institute Of Neurological Disorders And Stroke of the National Institutes of Health under Award Number R01NS120300. The content is solely the responsibility of the authors and does not necessarily represent the official views of the National Institutes of HealthWe thank the Allen Institute founder, Paul G. Allen, for his vision, encouragement, and support.

## Funding

National Institutes of Health grant R01 NS120300 (SYL, CAA)

## Contributions

Conceptualization: CAA; Methodology: SYL, FB, LC, TJ, CAA; Investigation: SYL, CAA; Visualization: SYL, CAA; Funding acquisition: SYL, CAA; Project administration: SYL, CAA; Supervision: CK, CAA; Writing – original draft: SYL, CAA; Writing – review & editing: SYL, FB, LC, TJ, CK, CAA

## Competing Interests

SYL consults for Starfish Neuroscience, Inc. CAA and SYL are listed as inventors on a patent application related to this work. CK is a Board Member and has a financial interest in Intrinsic Powers Inc.

**Figure 1**

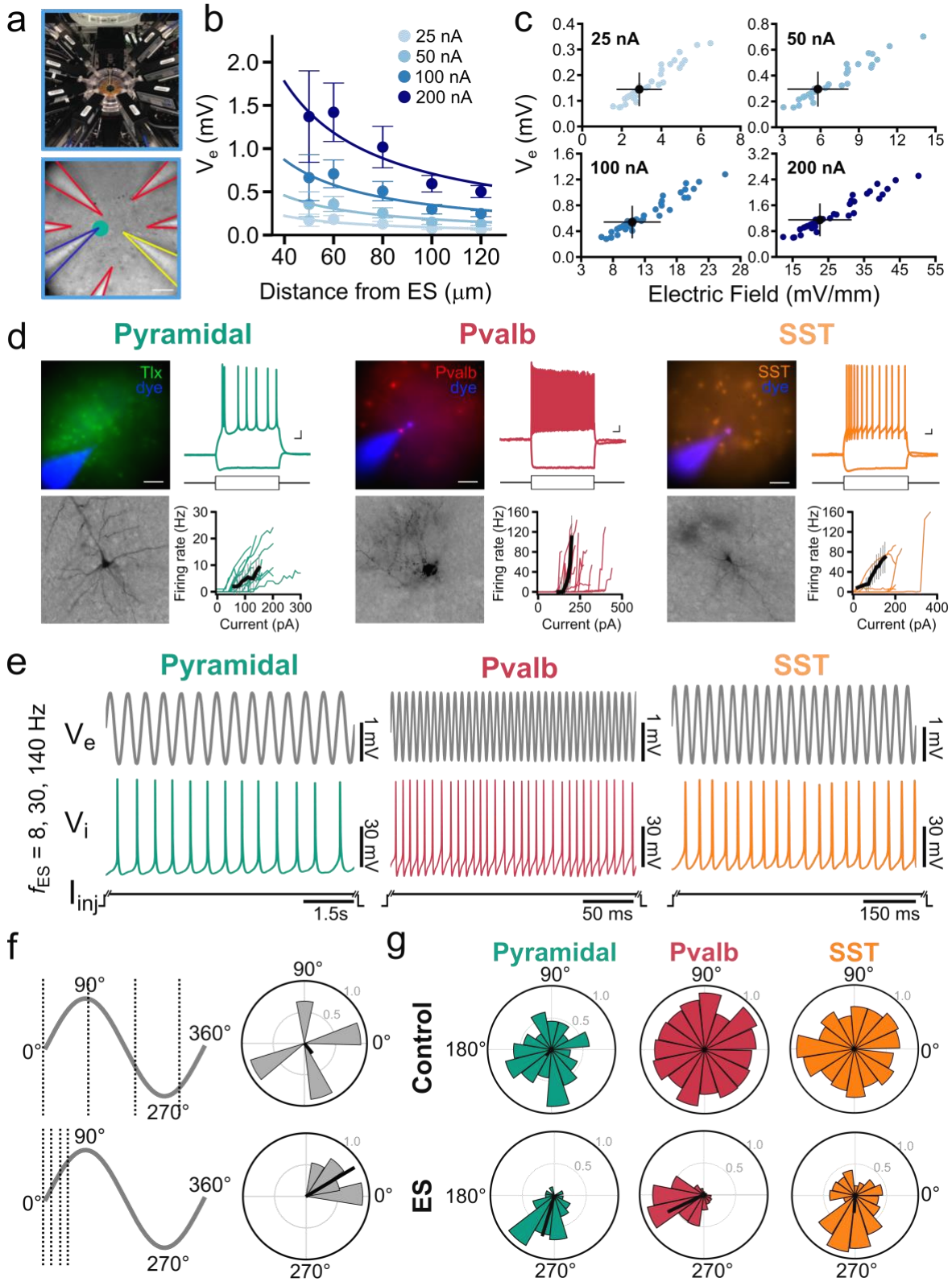
a
b
25 nA
50 nA
100 nA
200 nA
$V_e$ (mV)
Distance from ES (μm)
c
25 nA
50 nA
100 nA
200 nA
$V_e$ (mV)
Electric Field (mV/mm)
d
Pyramidal
Pvalb
SST
Tlx dye
Pvalb dye
SST dye
Firing rate (Hz)
Current (pA)
e
Pyramidal
Pvalb
SST
$V_e$
$V_i$
$I_{inj}$
$f_{ES}$ = 8, 30, 140 Hz
1 mV
30 mV
1.5s
50 ms
150 ms
f
90°
0°
360°
270°
g
Pyramidal
Pvalb
SST
Control
ES
180°

**Figure 1: Cellular and cell type-specific characterization of ES effects. a**, Top: Simultaneous ES, $V_i$ and $V_e$ recordings from eight electrodes near the soma of a whole-cell patched neuron. Bottom: Experiment in mouse cortical slice (yellow: extracellular ES, green: patched cell soma of layer 5 pyramidal neuron; blue: intracellular electrode recording $V_i$; red: extracellular electrodes recording $V_e$ at multiple locations within 150 um from soma). **b**, Left: $V_e$ amplitude as function of distance between ES and recording electrodes (ES: amplitude is 25-200 pA; ES frequency: 8 Hz; circles: $V_e$ mean amplitude; error bars: $V_e$ amplitude st.d.) Trendlines are least-squares fit of the point source approximation. **c**, $V_e$ and electric field amplitude elicited by the ES at the extracellular recording electrode closest to the whole-cell patched soma (approx. 15 µm). Blue: $V_e$ amplitude for each experiment (n=59); Black: mean and st.d. across experiments. **d**, Sample fluorescent images, cellular morphology, electrophysiology responses and resulting f-I curves from identified neocortical cells (colored lines: individual neurons; black: median). Three cell types: (left) excitatory pyramidal, (middle) inhibitory Pvalb, and (right) inhibitory SST. **e**, Experiments with simultaneous ES (delivered at 8, 30, and 140 Hz for all cells) and intracellular DC current injection $I_{inj}$ to elicit spiking. Sample electrophysiology traces from three cells. top, $V_e$ close to the soma; bottom: $V_i$ from inside the soma of a spiking neuron responding to $I_{inj}$ (5 s of $I_{inj}$ shown here). Left to right: traces from a pyramidal, a Pvalb and an SST neuron. **f**, Spikes are ascribed a phase by mapping the spike time to the $V_e$ phase from the electrode closest to the spiking cell. Spike phase distributions are shown in polar plots. **g**, Top: Polar plots of the spike-phase distribution for a pyramidal cell (green), Pvalb cell (red), and SST cell (orange) in the absence (Control) and presence of ES (200 pA; 8 Hz, 140 Hz, 30 Hz ES for pyramidal, Pvalb, and SST cells, respectively). The population vector length (black line) reflects the degree of entrainment. The presence of ES skews the spike-phase distribution and entrains the neurons. Bottom: Spike phase distributions under ES for a pyramidal (green; ES: 200 pA, 8 Hz), a Pvalb (red; ES: 200 pA, 140 Hz) and an SST neuron (yellow, ES: 200 pA, 30 Hz). # of spikes, Pyr: Control: 52, ES: 56; Pvalb: Control: 702, ES: 864; SST: Control: 216, ES: 218.

**Figure 2**

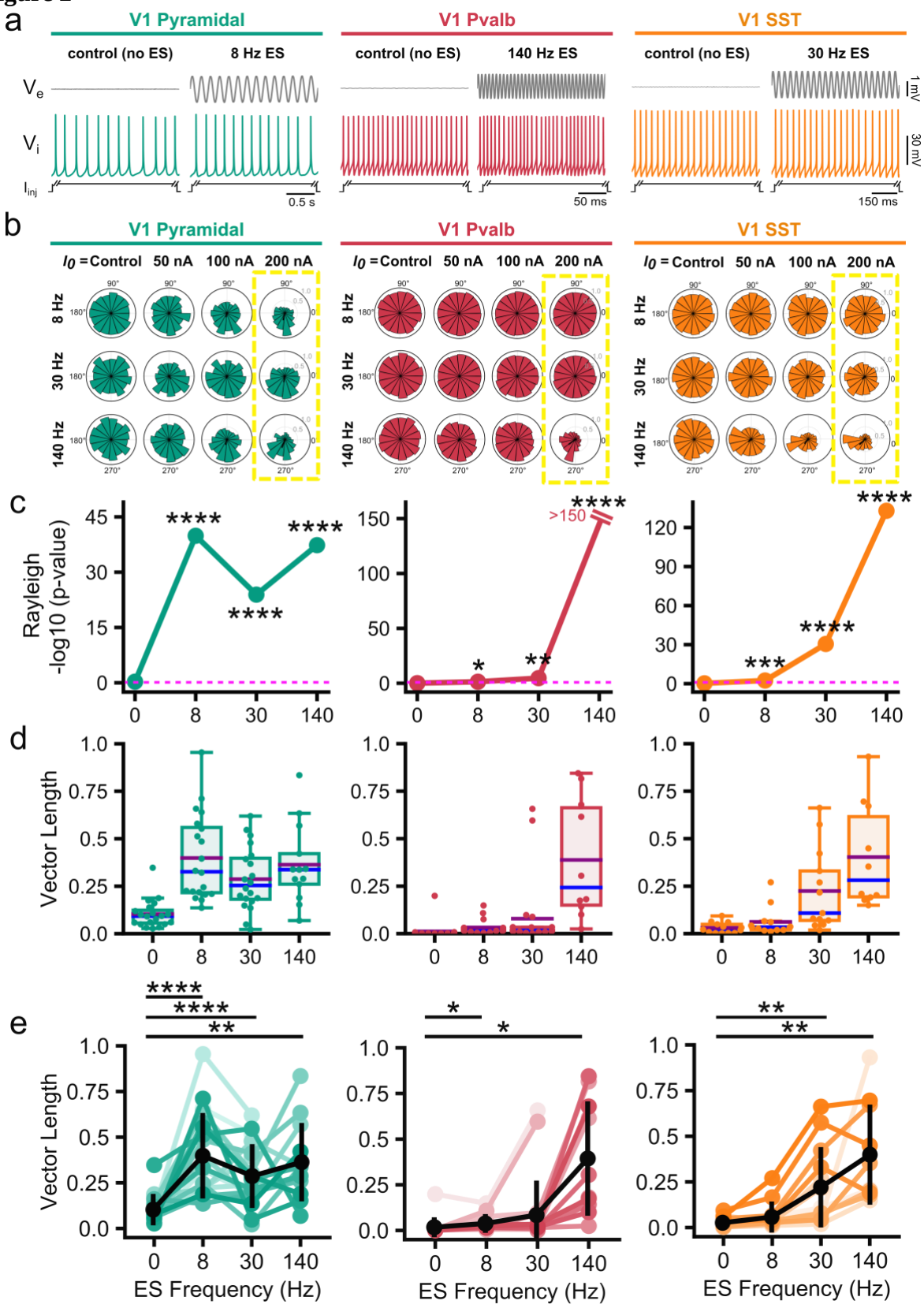
a
V1 Pyramidal
V1 Pvalb
V1 SST
control (no ES)
8 Hz ES
140 Hz ES
30 Hz ES
Ve
Vi
Iinj
1 mV
30 mV
0.5 s
50 ms
150 ms
b
I0 = Control
50 nA
100 nA
200 nA
8 Hz
30 Hz
140 Hz
c
Rayleigh
-log10 (p-value)
>150
d
Vector Length
e
ES Frequency (Hz)

**Figure 2. Cell class-specific entrainment of spiking to ES**. **a,** Simultaneous spiking induced by a suprathreshold DC stimulus $I_{inj}$ co-occurs with sinusoidal ES. Despite its relatively small amplitude (see Figure 1c and Figure 2), the subthreshold effect entrains neuronal spike timing (left to right: traces from a pyramidal, a Pvalb and an SST neuron) without affecting the spike rate (see Figure S1). **b**, Spike-phase distribution for pyramidal (green), Pvalb (red), and SST (orange) cell classes for varying ES parameters. (Rows) ES frequency (top to bottom): 8, 30, to 140 Hz. (Columns) ES amplitude (left to right): 0 (Control), 50, 100 and 200 nA. "Control" indicates no ES is applied (ES amplitude: 0 nA). Control experiments show symmetric spike-phase distribution, i.e., no inherent preferred spike-phase in the absence of ES, as assessed by Rayleigh's test ($p>0.05$, see Table S2). Increasing (but subthreshold) ES amplitude generally increases spike-phase entrainment. Different ES frequencies have a distinct, cell class-specific effect on spike phase entrainment. Summary statistics for the highest amplitude (in yellow box) plotted in **c**. **c-e,** Spike entrainment to ES assessed via the Rayleigh's test (**c**) and the population vector length (**d-e**) against the ES frequencies (ES amplitude: 200 nA). **c,** p-values calculated for pyramidal, Pvalb, SST spikes (left to right) via Rayleigh's test as function of ES frequency show statistically significant spike phase entrainment (*$p < 0.05$, **:$p < 0.01$, ***$p < 0.001$, ****$p < 0.0001$, see Table S2). Dashed pink line indicates p-value at 0.05. Pyramidal spiking entrains to slow (8 Hz), medium (30 Hz), and fast (140 Hz) ES frequencies while Pvalb and Sst are most strongly entrained by high ES frequencies (140 Hz). **d**, The population vector length plotted for each cell (gray circles) within each class (left to right: Pyramidal, Pvalb, SST). Purple and blue lines: mean and median values, respectively; error bars: st.d. **e**, The population vector length for each cell (from **d**) across each ES frequency is compared against control conditions (no ES) to assess degree of entrainment (paired t-test, false discovery rate (FDR)-corrected for multiple comparisons: *$p<0.05$, **$p<0.01$, ****$p<0.0001$) Pyramidal: N=21 cells for 8, 30 Hz, N=13 for 140 Hz; Pvalb: N=22 cells for 8, 30 Hz, N=12 for 140 Hz; Sst: N=13 for 8, 30 Hz, N=10 for 140 Hz.

**Figure 3**

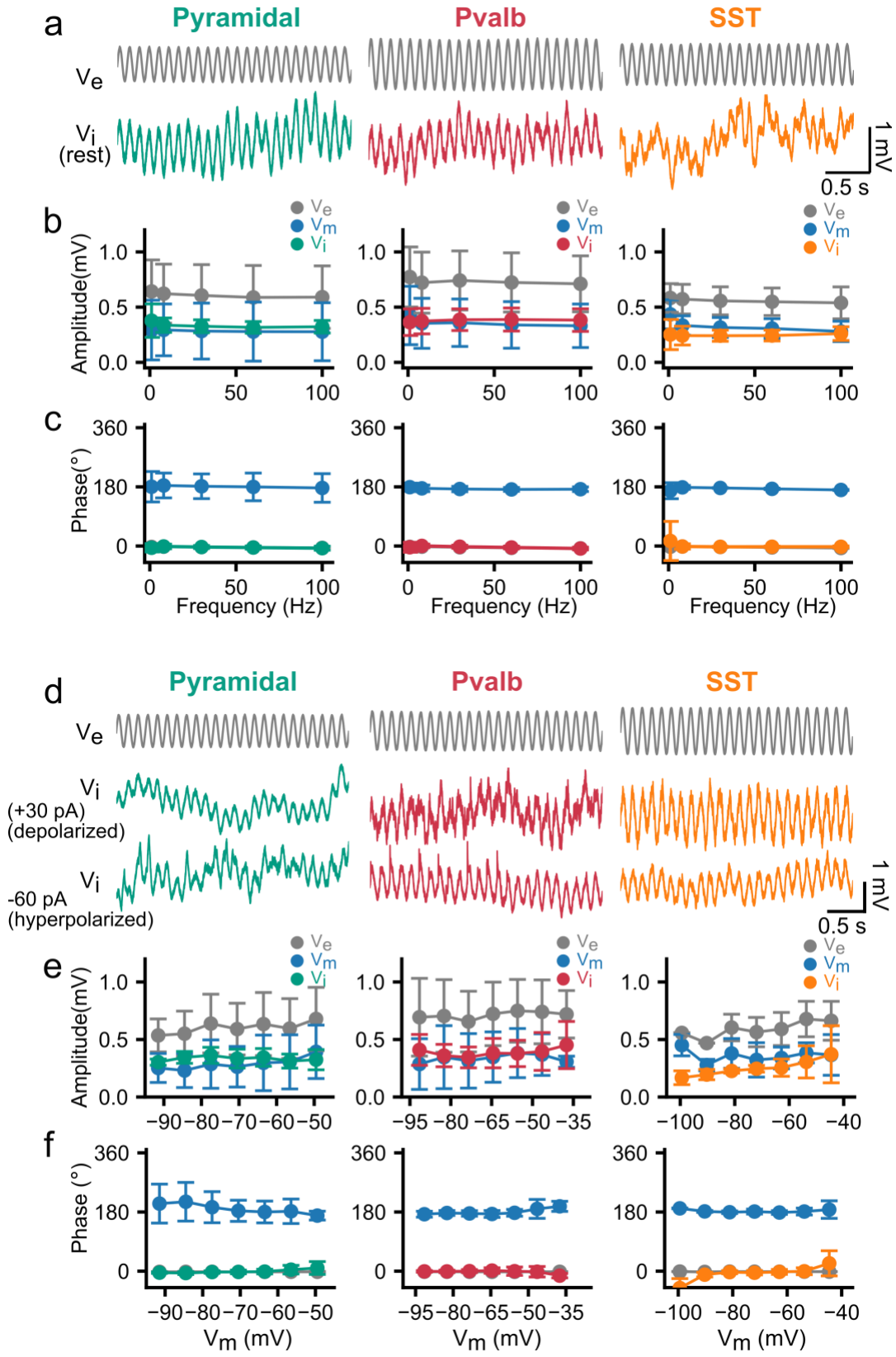
a
Pyramidal
Pvalb
SST
Ve
Vi
(rest)
1 mV
0.5 s
b
Amplitude(mV)
Ve
Vm
Vi
c
Phase(°)
Frequency (Hz)
d
(+30 pA)
(depolarized)
-60 pA
(hyperpolarized)
e
f
Phase (°)
Vm (mV)

**Figure 3. Non-specific, ES frequency-independent subthreshold entrainment of excitatory and inhibitory cell classes to ES. a**, Entrainment of $V_i$ to ES, for pyramidal (green), Pvalb (red), and SST (orange) cells. Gray traces: $V_e$ measured at the closest extracellular location (15 µm) from the cell soma. The subthreshold sinusoidal ES is delivered 50 µm from cell soma (frequency: 8 Hz, amplitude: 100 nA). **b,c,** ES effect on neurons at resting potential (ES amplitude: 100 nA, frequency: 1 to 100 Hz). Amplitude (**b**) and phase (**c**) of the ES where $V_e$ (gray), $V_i$ (green, red, or orange), and $V_m$ (blue) for each cortical cell type (circles: mean; error bars: std; left to right: pyramidal, Pvalb; right: SST). The three cell classes exhibit ES frequency independence with induced $V_i$, $V_e$ and $V_m$ amplitude and phase remaining constant for ES frequencies ranging 1-100 Hz (one-way ANOVA, $p>0.05$ for Pyr, Pvalb, and SST). **d**, ES effect on hyper- and depolarized neurons held at a range of membrane potentials via injection of depolarizing or hyperpolarizing current $I_{inj}$ (from -90 to 90 pA). The sinusoidal ES is simultaneously applied with $I_{inj}$ (ES amplitude: 100 nA, frequency: 8 Hz). **e,f** Amplitude (**e**) and phase (**f**) of the ES-induced $V_e$ (gray), $V_i$ (green, red, or orange), and $V_m$ (blue) for each cortical class for hyper- and depolarizing $I_{inj}$ (circles: mean; error bars: std; left to right: pyramidal, Pvalb; right: SST). The induced ES effect on $V_i$, $V_e$ and $V_m$ amplitude and phase are broadly independent of membrane polarization and remain constant across a range of 40 mV for the three classes. N=24 cells (Pyramidal), N=22 cells (Pvalb), N=6 cells (SST).

**Figure 4**

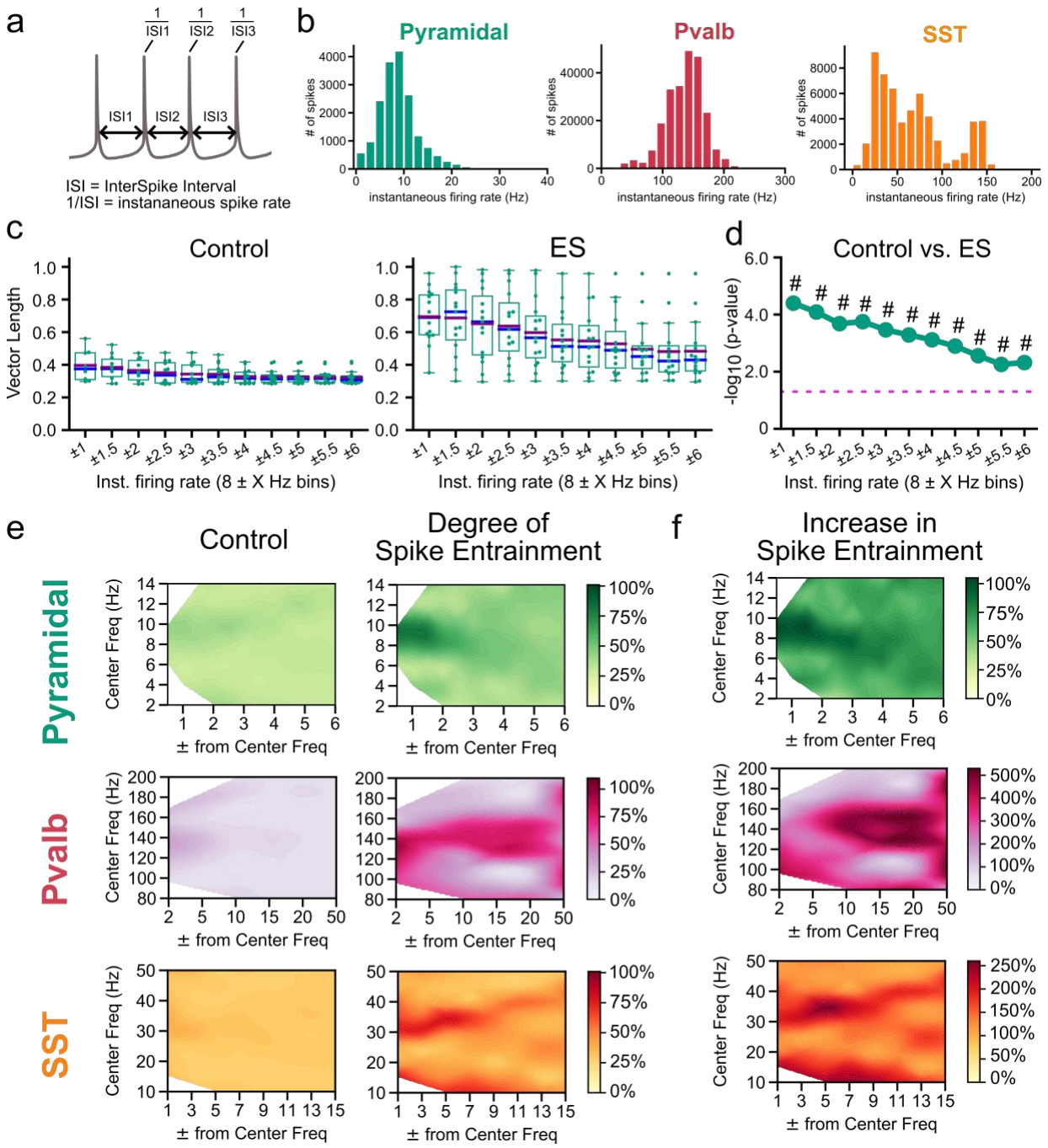
a
1/ISI1
1/ISI2
1/ISI3
ISI1
ISI2
ISI3
ISI = InterSpike Interval
1/ISI = instananeous spike rate
b
Pyramidal
Pvalb
SST
# of spikes
instantaneous firing rate (Hz)
c
Control
ES
Vector Length
Inst. firing rate (8 ± X Hz bins)
d
Control vs. ES
-log10 (p-value)
Inst. firing rate (8 ± X Hz bins)
e
Control
Degree of Spike Entrainment
f
Increase in Spike Entrainment
Pyramidal
Pvalb
SST
Center Freq (Hz)
± from Center Freq

**Figure 4. Cell class-specific ES entrainment of spiking correlates with spike rate properties of the individual classes. a**, Schematic diagram demonstrating the instantaneous spike rate for each spike, calculated as the inverse of the interspike interval (ISI). ISI: time between a spike and the next consecutive spike. **b**, Histogram of the instantaneous spike rate distribution for all spikes recorded in pyramidal (green), Pvalb (red), and SST (orange) cell classes. (N=21 cells (Pyramidal), N=22 cells (Pvalb), N=13 (SST)). **c**, Degree of spike entrainment (as evaluated by population vector length) to ES applied at 8 Hz and 200 nA, plotted for each recorded cell's spikes in the pyramidal class and containing only spikes firing within a specific spike-rate range/bin. Bootstrap means of spikes within each cell were obtained with 10000 trials. Bin size (boundaries) are designated by the spike rate to be analyzed (a "Center" Frequency) plus or minus differing values (ranging from ±1 to ±6 Hz). Broader spike-frequency ranges are on the left, with the bin size narrowing towards the right. Boxplots show the quartiles of the dataset and whiskers the remaining distribution. Purple and blue lines: mean and median values, respectively. **d,** Plot of $-\log_{10}$ p-values (Welch's t-test; null-hypothesis: the two populations have equal means) for comparison between the same-spike-range bins (e.g., 8±1 Hz Control vs 8±1 Hz ES bins) between Control vs. ES (in **c**)). Dashed pink line shows $p$=0.05 and # indicates effect size (via Cohen's d) where # indicates d>0.8. **e,** Heat maps show degree of spike entrainment (expressed as % of the normalized vector length, 0-1) to Control (no ES; left column) or ES application for spikes within specific spike-rate bins, in pyramidal (green), Pvalb (red), and SST (orange) cell classes (right column). Results are shown for ES (200 nA) at 8 Hz for pyramidal, 140 Hz for Pvalb, and 30 Hz for SST. Bin size (boundaries) is designated by first examining the spike rate to be analyzed (a "Center" Frequency) plus or minus differing values (as in **c**), and then also by varying the "center frequency" itself. **f**, Heap map representing the increase in spike entrainment in **e**, during ES application vs. during Control (as calculated by dividing the values during ES application by Control values) for pyramidal, Pvalb, and SST classes. (N=21 cells for 8, 30 Hz and N=13 for 140 Hz (Pyramidal), N=22 cells for 8, 30 Hz and N=12 for 140 Hz (Pvalb), N=13 for 8, 30 Hz and N=10 for 140 Hz (SST)).

**Figure 5**

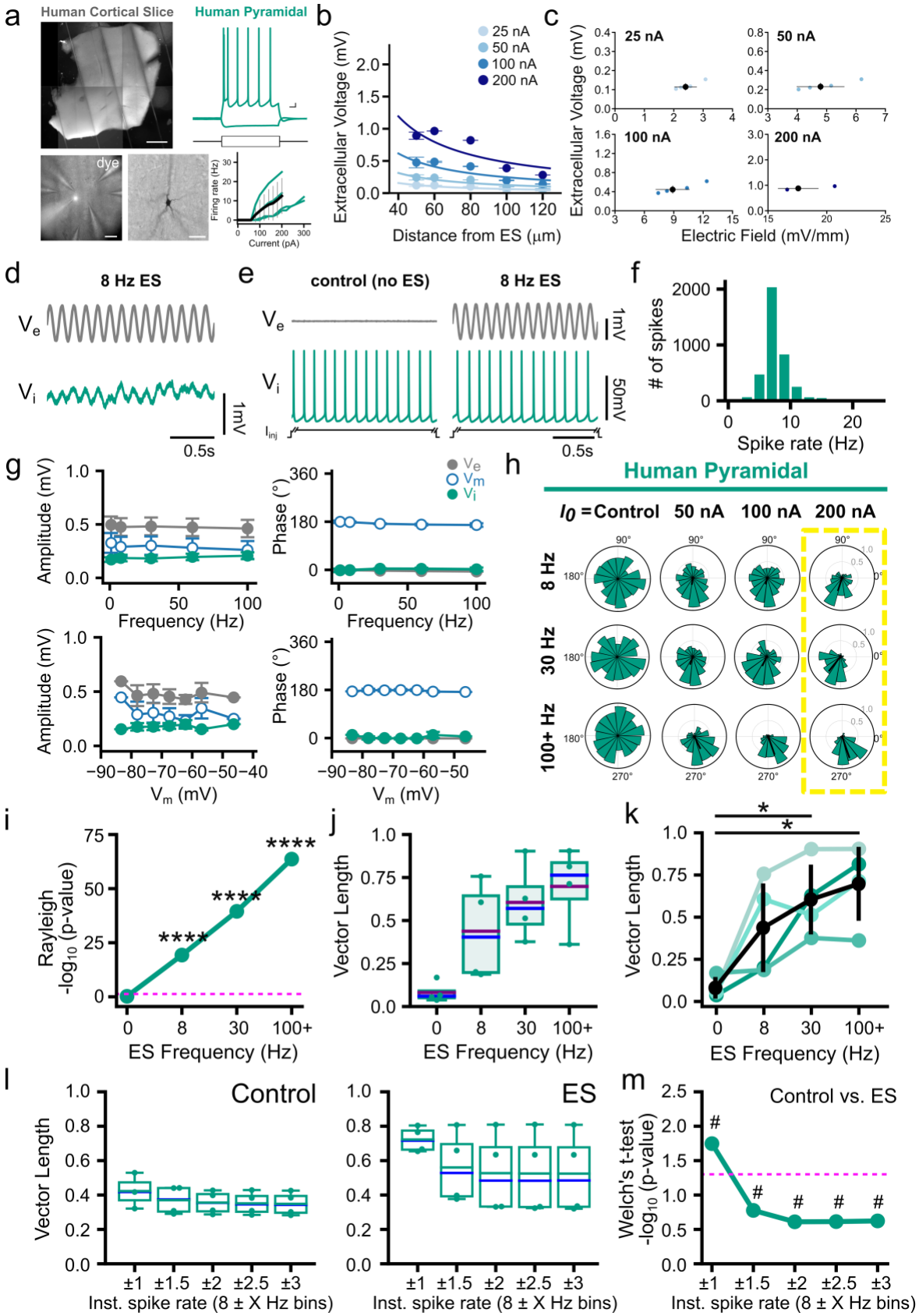
a
Human Cortical Slice
Human Pyramidal
dye
Firing rate (Hz)
Current (pA)
b
25 nA
50 nA
100 nA
200 nA
Extracellular Voltage (mV)
Distance from ES (μm)
c
25 nA
50 nA
100 nA
200 nA
Extracellular Voltage (mV)
Electric Field (mV/mm)
d
8 Hz ES
Ve
Vi
1mV
0.5s
e
control (no ES)
8 Hz ES
Ve
Vi
Iinj
1mV
50mV
0.5s
f
# of spikes
Spike rate (Hz)
g
Amplitude (mV)
Phase (°)
Ve
Vm
Vi
Frequency (Hz)
Vm (mV)
h
Human Pyramidal
I0 =Control
50 nA
100 nA
200 nA
8 Hz
30 Hz
100+ Hz
i
Rayleigh
-log10 (p-value)
ES Frequency (Hz)
j
Vector Length
ES Frequency (Hz)
k
Vector Length
ES Frequency (Hz)
l
Control
ES
Vector Length
Inst. spike rate (8 ± X Hz bins)
m
Control vs. ES
Welch's t-test
-log10 (p-value)
Inst. spike rate (8 ± X Hz bins)

**Figure 5. Sub- and Suprathreshold ES entrainment of human neurons. a**, Top (left): Human *ex vivo* cortical slice obtained via neurosurgical tissue resections. (right) Sample electrophysiological firing trace of human pyramidal neuron after depolarizing and hyperpolarizing current injections. Bottom (left): Human cortical slice with extracellular electrodes recording $V_e$ at multiple locations within 50-120 µm from pyramidal soma (white spot: soma of recorded cell filled with biocytin and dye for identification). (middle): Pyramidal cell morphology of recorded cell visualized with post-hoc biocytin-HRP staining. (right): f-I curves of recorded cells. **b,** Left: $V_e$ amplitude as function of distance between ES and recording electrodes (ES: sinusoidal stimulus amplitude is 25-200 pA; ES frequency: 8 Hz; circles: $V_e$ mean amplitude; error bars: $V_e$ amplitude st.d.) Trendlines are least-squares fit of the point source approximation. **c**, $V_e$ and electric field amplitude elicited by the ES at the extracellular recording electrode closest to the whole-cell patched soma (approx. 15 µm). Blue: $V_e$ amplitude for each experiment (n=5); Black: mean and st.d. across experiments. **d,** Sample trace of a human pyramidal neuron showing **e**ntrainment of $V_i$ (green trace) to subthreshold ES. $V_e$ (gray trace) measured at the closest extracellular location (15 µm) from the cell soma. The subthreshold sinusoidal ES is delivered 50 µm from cell soma (frequency: 8 Hz, amplitude: 100 nA). **e,** Simultaneous spiking induced by a suprathreshold DC stimulus $I_{inj}$ that co-occurs with sinusoidal ES in human neurons. Despite its relatively small amplitude (see also **c**), this subthreshold-level ES affects neuronal spike timing without inducing spike generation. **f,** Spike rate distribution for all spikes recorded from the human pyramidal neurons (N=4 cells). **g,** Subthreshold ES effect at resting potential (top) and at hyper- and depolarized potentials (bottom). Neurons were held at a range of membrane potentials via injection of depolarizing or hyperpolarizing current $I_{inj}$ (from -90 to 90 pA). (ES amplitude: 100 nA, frequency: 1 to 100 Hz). Amplitude (left) and phase (right) of the ES are shown, with $V_e$ (gray), $V_i$ (green), and $V_m$ (blue outlined circle). (circles: mean; error bars: std). Human pyramidal neurons exhibit ES-frequency independence with induced $V_i$, $V_e$ and $V_m$ amplitude and phase remaining constant for ES frequencies ranging 1-100 Hz. The induced ES effect on $V_i$, $V_e$ and $V_m$ amplitude and phase remain constant across a range of 40 mV polarization. **h,** Spike-phase distribution for varying ES parameters. (Rows) ES frequency (top to bottom): 8, 30, to 100+ Hz. (Columns) ES amplitude (left to right): 0 (Control), 50, 100 and 200 nA. "Control" indicates no ES is applied (ES amplitude: 0 nA) and show symmetric spike-phase distribution as assessed by Rayleigh's test ($p>0.05$, see Table S4). Increasing ES amplitude increases spike-phase entrainment across slow (8 Hz), medium (30 Hz), and fast (100+ Hz) ES frequencies. **i-k,** Summary statistics for the highest amplitude (200 nA, yellow box in h). **i,** Spike entrainment to ES assessed via Rayleigh's test versus ES frequency show statistically significant spike phase entrainment (****$p < 0.01$; dashed pink line: $p$=0.05). **j**, The population vector length plotted for each cell. Purple and blue lines: mean and median values, respectively; error bars: st.d. **k**, The population vector length for each cell (from **j,** each line represents a cell) across ES frequencies (paired t-test, false discovery rate (FDR)-corrected for multiple comparisons: *$p<0.05$, see Table S4). **l,** Degree of spike entrainment (as evaluated by population vector length) to Control (i.e. no ES, left) or to ES applied at 8 Hz and 200 nA (ES, right), plotted for each recorded human pyramidal cell, containing only spikes firing within a specific spike-rate range/bin. Bootstrap means of spikes within each cell obtained with 10000 trials. Bin size (boundaries) are designated by the spike rate to be analyzed (a "Center" Frequency) plus or minus differing values (ranging from ±1 to ±6). **m,** Plot of $-\log_{10}$ p-values (Welch's t-test) for comparison between the same-spike-range bins

(e.g. 8±1 Hz Control vs 8±1 Hz ES bins) between Control vs. ES (in **k**). Dashed pink line indicates p-value at 0.05 and # indicates effect size (via Cohen's d) where # indicates d>0.8.

## Methods

Acute Slice preparation:

Mouse and human tissue were prepared with slice preparation reagents and protocols standardized at the Allen Institute [65].

Acute mouse brain slices, from both female and male mice at ages P40-P50, were prepared as described in [66]. All mouse procedures were approved by the Allen Institute's Institutional Care and Use Committee. Mice were anesthesized with 5% isoflourane and transcardially perfused with ice-cold, oxygenated artificial cerebrospinal fluid solution (ACSF.I[65]): in mM: 0.5 $CaCl_2 \cdot 2H_2O$, 25 D-glucose, 98 HCl, 20 4-(2-hydroxyethyl)-1-piperazineethanesulfonic acid (HEPES), 10 $MgSO_4 \cdot 7H_2O$, 1.25 $NaH_2PO_4$, 3 myo inositol, 12 N-acetylcysteine, 96 N-methyl-D-glucamine (NMDG), 2.5 KCl, 25 $NaHCO_3$, 5 Na-L-ascorbate, 3 Na-pyruvate, 0.01 taurine, 2 thiourea). Parasagittal cortical slices (350 µm) were prepared in ACSF.I with a Compresstome (Precisionary Instruments) or VT1200S Vibratome (Leica Biosystems), and the slicing angle was set to 17 degrees relative to the sagittal plane to preserve aprical dendrites of pyramidal cells. Hippocampal slices were sliced in the coronal plane. Slices were kept in a recovery chamber containing oxygenated ACSF.I for 10 minutes at 34ºC. They were then transferred to a holding chamber containing oxygenated ACSF.IV[65], consisting of the following (in mM): 2 $CaCl_2 \cdot 2H_2O$, 25 D-glucose, 20 HEPES, 2 $MgSO_4 \cdot 7H_2O$, 1.25 $NaH_2PO_4$, 3 myo inositol, 12.3 N-acetyl-L-cysteine, 2.5 KCl, 25 $NaHCO_3$, 94 mM NaCl, 5 Na-L-ascorbate, 3 mM Na-pyruvate, 0.01 taurine, 2 thiourea. Slices were kept in the holding chamber (at least one hour) at room temperature until time of recording.

Acute human cortical slices were prepared as described in [67]. All procedures involving human tissue are reviewed by the review boards at the hospitals performing the surgeries before beginning the study, and all patients provided informed consent. Tissue was extracted from the temporal or frontal lobe of patients undergoing neurosurgery for epilepsy or tumors (mean age: 27 ± 13.8 years, 3 donors). The tissue specimens were distal to the core pathological site and was deemed not to be of diagnostic value. The specimens were placed in a sterile container filled with pre-chilled, carbogenated aCSF VII[65] (in mM: 0.5 $CaCl_2 \cdot 2H_2O$, 25 D-glucose, 92 HCl, 20 HEPES, 10 $MgSO_4 \cdot 7H_2O$, 1.2 $NaH_2PO_4$, 92 NMDG, 2.5 KCl, 30 $NaHCO_3$, 5 Na-L-ascorbate, 3 mM Na-pyruvate, 2 thiourea). Specimens were transported from the surgical site to the laboratory within 10-40 min, where they were trimmed and mounted for best preserving intact cortical columns (pial surface to white matter) during slicing. Specimen were sliced in aCSF VII using a Compresstome or Vibratome and transferred to a holding chamber containing oxygenated aCSF VII at 34°C for 10 min, then moved and kept in aCSF IV[65] (REF) at room temperature for a minimum of one hour before recording began.

Electrophysiology and analysis

Rig setup:

Recordings were performed in a customized multi-patch system, as described in [66]. The multi-patch system consists of 8 headstages with pipettes arranged in a semi-circular organization, as seen in Figure 1a, and allows for simultaneous intra- and extracellular stimulation and recordings at multiple locations close by cell soma. One pipette was used for the intracellular stimulation and recordings, one for extracellular stimulation, and the rest were placed within 50-120 $\mu m^3$ of each cell soma to record the extracellular voltage. The electrode distance and placement (within +/- 5µm) was measured with Acq4 software [68], which was connected to the microscope and micromanipulators for providing accurate tracking of the

hardware and cell position. The pipette holders were equipped with customized metal shields to reduce crosstalk artifacts. Each headstage was controlled independently through modified triple-axis motors (Scientifica; PatchStar). Intracellular and extracellular stimulation was applied through Multiclamp 700B amplifiers (Molecular Devices). (Intracellular and extracellular stimulation was applied through different amplifers). Data acquisition was conducted using Multi-channel Igor Electrophysiology Suite (MIES; https://github.com/AllenInstitute/MIES), custom software written in Igor Pro (WaveMetrics). Recorded signals were amplified with a Multiclamp 700B amplifier and digitized at 50-200 kHz with ITC 1600 DAQs. (Heka). Pipette pressure was regulated using both electro-pneumatic control valves (Proportion-Air; PA2193) under control of MIES software, and through manual (via mouth) pressure. Slices were visualized through an upright microscope (BX61WI, Olympus) with oblique infrared illumination (WI-OBCD condenser) equipped with 4X and 40X objectives, on a custom motorized stage (Scientifica), and images were taken with a digital sCMOS camera (Hamamatsu; Flash 4.0 V2). Acq4 software[68] was also used for imaging, and subsequent image analysis.

Cell class identification and characterization

In mouse recordings, individual neuronal cell classes were identified by the following methods: Excitatory pyramidal cells were identified with Cre- or Flp-dependent transgenic mice with fluorescent reporters (TdTomato or eGFP) specific for Layer 5 excitatory neurons (through Tlx3 or Sim1 promoters) or by their pyramidal morphology (in V1 and hippocampus). They were confirmed by their regular-spiking firing pattern (in response to intracellularly injected current steps) in patch-clamp recordings. Inhibitory Pvalb and SST cells were identified with Cre- or Flp-dependent transgenic mice with fluorescent reporters (TdTomato or eGFP) specific for Pvalb or SST cell classes (though Pvalb or SST promoters), and confirmed by their fast-spiking firing pattern. The intracellular recording pipette was filled with dye (Cascade Blue) to confirm overlap between the recorded cell and fluorescence to ensure proper cell class targeting. In human neuron recordings, pyramidal classes in Layer 5 were targeted by their location (approximately 1800 mm from pia [69]), large size and clear apical dendrites, and then confirmed by their regular-spiking firing pattern (in response to intracellularly injected current steps) in patch-clamp recordings.

After recordings, the slices underwent *post-hoc* processing to confirm cortical layer boundaries (via 4',6-diamidino-2-phenylindole (DAPI) staining) and to reveal their cellular morphology (via biocytin labeling). Slices were first processed for immunohistochemistry by fixation in 4% paraformaldehyde and 2.5% glutaraldehyde for at least 40 hours at 4°C, then transferred and washed in phosphate buffer saline (PBS) for 1-7 days. Slices were then placed in 5 μM DAPI in PBS for 15 min at room temperature and then washed three times in PBS. Slices were then transferred to 1% hydrogen peroxide ($H_2O_2$) in PBS to extinguish endogenous peroxidases for 30 min, and then washed three times in PBS. For biocytin labeling, a 3,3'-diaminobenzidine (DAB) peroxidase substrate kit (Vector Laboratories) was used. Slices were mounted and dried for approximately 2 days before imaging on an AxioImager Z2 microscope (Zeiss) equipped with an Axiocam 506 monochrome camera (Zeiss) at 20X, with images acquired via the Zeiss Efficient Navigation software.

Electrophysiological recordings

Electrophysiological recordings were performed in slices (for both mouse and human slices) at 32-34 °C perfused under carbogenated recording ACSF (aCSF.IX[65] (in mM: 1.3 $CaCl_2 \cdot 2H_2O$, 25 D-glucose, 1 $MgSO_4 \cdot 7H_2O$, 1.2 $NaH_2PO_4$, 3 KCl, 18 $NaHCO_3$, 126 NaCl, 0.16

Na-L-ascorbate). In order to examine the effects of ES without potentially confounding factors of synaptic activity, recordings were conducted in the presence of synaptic blockers. Synaptic transmission blockers kynurenic acid (1 mM, Sigma) and gabazine (10 μM, Tocris) were added to the aCSF to block fast glutamatergic and GABAergic synaptic activity, respectively. Whole-cell patch-clamp recordings were performed with internal solution containing 130 K-gluconate, 10 HEPES, 0.3 ethylene glycol-bis(β-aminoethyl ether)-N,N,N',N'-tetraacetic acid (EGTA), 3 KCl, 0.23 $Na_2GTP$, 6.35 $Na_2$Phosphocreatine, 3.4 Mg-ATP, 13.4 Biocytin, and 50 μM Cascade Blue dye (excited at 490 nm), 280-295 mOsm and pH 7.2-7.3. (Electrophysiological values are reported without liquid junction potential correction). Pipettes for extracellular stimulation and voltage recordings contained aCSF IX. Patch pipettes were pulled from borosilicate glass capillaries (Sutter Instruments) with a DMZ Zeitz-Puller (Zeitz), with tip resistances of 4-6 MΩ for whole-cell recordings and 1-2 MΩ for extracellular stimulation and voltage recordings.

Whole-cell patch-clamp recordings were performed on neurons that had a stable seal (>1 GΩ) and successful break-in. Bridge balance was monitored and did not exceed 15 MΩ. Resting membrane potential (RMP) was measured at 1-2 minutes after break-in of the cell, and only neurons with RMP over -53 mV were recorded. Bias current was injected within the MIES software package for the remainder of the experiment to maintain the determined resting membrane potential. To examine the cell-class-specific firing pattern and intrinsic properties of the recorded cell, and to generate the F-I (frequency-current) curve, intracellular current steps were injected into the cell at current-clamp mode. 20 pA steps (1 second) from -160 pA up to 200 pA were applied to the cell for all cell classes), and in further steps up to 400 pA for cells with a higher spike threshold. The rheobase was determined by the minimum current amplitude needed to generate an action potential (AP). The interspike interval (ISI), the difference in time between an APl and the next subsequent AP, was used to calculate the cell firing rate. AP threshold was calculated by first identifying the membrane voltage deflection point at which the first-order derivative of the membrane potential (dV/dt) exceeded 20mV/ms, and adjusted to where the dV/dt was 5% of the average maximal dV/dt. Input resistance was calculated by first plotting the voltage vs. the injected current at the hyperpolarizing steps from -120 pA to 20 pA, and then taking the slope of the resulting fit.

Subthreshold entrainment and analysis

In order to analyze the effect of ES on subthreshold cellular dynamics, we recorded from neurons under current-clamp mode, while delivering ES of varying amplitude (25-200 nA) and frequency (1-100 Hz) for 5 seconds. Neurons were either held at their resting potential, or at varying subthreshold polarization levels (through intracellular current delivered through the pipette 30 pA steps, from -90 pA to 90 pA). To calculate the resulting amplitude, frequency and phase of the extracellular ($V_e$), intracellular somatic ($V_i$), and the resulting membrane voltage ($V_m$, calculated as $V_m=V_i-V_e$), we first divided the raw unfiltered trace into [0, T]-timed intervals, where T (in seconds) represents the period of the ES as defined by T = 1/frequency. (e.g. for an 8 Hz stimulus, T = 0.125 s (1/8 Hz), which results in 40 intervals (5 s / T) for a 5 second stimulus duration). We then aligned these intervals to determine the mean waveform by calculating the mean of the aligned interval traces from 0 to T. The $V_e$ trace used was from extracellular electrode closest to the cell soma (15 mm away), and the $V_i$ trace was from the intracellular recording electrode. The amplitude, frequency and phase of the mean waveform of each neuron from each recording was extracted for the analysis of subthreshold neuronal entrainment in Figure 2.

Spike entrainment and analysis

To examine the effects of ES on the suprathreshold properties of neurons, we injected intracellular DC current into neurons under current-clamp mode, to elicit action potentials during a 9 second intracellular stimulation protocol. Neurons were held at their resting membrane potential, and the DC current was first injected into the neurons in the absence of ES ("Control" condition), and then same DC current was injected into the neurons while concurrently applying ES at varying frequencies (8-140 Hz) and amplitudes (25 to 200 nA). (DC current amplitude was determined as the current injection necessary to sustain spiking during the protocol) For the spike-phase calculation, i.e. the phase of the extracellular *V*e when an action potential is elicited, the $V_e$ trace was first bandpass-filtered with frequency limits from 0.5 Hz to 200 Hz. The $V_e$ trace used was from extracellular electrode closest to the cell soma (15 mm away). We then used the Hilbert transform to calculate the instantaneous phase of the oscillating $V_e$, closest to the cell soma during spiking. The phase (in degrees) was measured in the range 0° to 360°, with 90° the peak and 270° the trough of the $V_e$ waveform. Traces were analyzed after the first 0.5 s of the protocol to ensure stability of cell spiking for analysis. Spike time for each action potential was measured individually for each spike at the voltage deflection point at which the first-order derivative of the membrane potential (dV/dt) exceeded 20 mV/ms. The spike phase is thus defined as the instantaneous $V_e$ phase at the spike time. Spike times were also used to count and compare the number of spikes during Control vs. ES-application conditions.

We examined the spike phases during the ES via circular statistics (with the ES-modulated $V_e$ as reference) to determine whether a neuron was significantly phase locked. The Rayleigh test was used to assess the uniformity of spike-phase distribution (null hypothesis: distribution is uniform), and population-vector analysis was used to examine whether spikes exhibit a preference to any specific phase of the imposed $V_e$. The spike distribution during control (i.e. no ES) experiments was examined during alignment to a "virtual" (using the $V_e$ from the subsequent ES experiment) extracellular field and compared to the spike distribution of neurons during ES.

The relationship between spike rate and spike-field entrainment was examined in detail by taking the vector lengths of spike dataset per cell, and binning the spikes according to their instantaneous spike frequency (as calculated by the spike ISI). Bootstrap mean values for each cell in each cell class was obtained by shuffling the number of spikes in 10000 trials. The spike-frequency bins were constructed by taking the specific ES frequency inducing entrainment for each cell class (a "center frequency") and adjusting the bin width by adding/subtracting from the center frequency. The degree of entrainment (as assessed by vector length) for the specific spike-frequency bins, was determined by taking the values of the spike-frequency bins (during ES) and dividing them by the values of the spike-frequency bins during Control conditions.

Statistical analyses

Statistical analysis was performed was performed using Python in SciPy[70] and Circstat (https://github.com/circstat/pycircstat). Data was tested for normality (Shapiro-Wilk test), and for normally distributed data, we used the two-sided Welch's t-test or paired t-test. One-way ANOVAs were used to compare multiple frequencies in Figure 2, and the Cohen's test and Levene's test were used to examine effect size and homogeneity of variance, respectively, as indicated in the figures. Significance was determined at $p<0.05$, as denoted by the following: (* $p < 0.05$, **: $p < 0.01$, *** $p < 0.001$, **** $p < 0.0001$). Statistical tests performed with multiple comparisons are reported with false discovery rate (FDR)-corrected p-values using the Benjamini-Hochberg method. Values in the text are presented as mean ± standard deviation, or where as noted, also with median and interquartile ranges.